Nanoscale

PAPER

View Article Online
View Journal | View Issue

Cite this: *Nanoscale*, 2024, **16**, 11679

Finite size effects on the metamagnetic phase transition in a thick B2 FeRh nanocluster film†

Guillermo Herrera, *[a] Anthony Robert,[a] Sara Gonzalez,[b] Patrick Schoeffmann,[c] Alexandre Tamion,[a] Florent Tournus,[a] Laurent Bardotti,[a] Olivier Boisron,[a] Clément Albin,[a] Nicholas Blanchard,[a] Ingrid Canero-Infante, [b] Pedro Rojo Romeo,[b] Bruno Canut,[b] Edwige Otero,[c] Philippe Ohresser,[c] Fabrice Wilhelm,[d] Andrei Rogalev,[d] Matthieu Bugnet, [e] Damien Le Roy[a] and Véronique Dupuis [a]

Received 29th February 2024,
Accepted 22nd May 2024

DOI: 10.1039/d4nr00873a

rsc.li/nanoscale

FeRh alloys in the CsCl-type (B2) chemically ordered phase present an antiferromagnetic to ferromagnetic order transition around 370 K observed in bulk and continuous films but absent in nanoclusters. In this study, we investigate the thermal magnetic behavior of a thick film composed of assembled FeRh nanoclusters preformed in the gas phase. This work reveals a broad and asymmetric metamagnetic transition with a consequent residual magnetization at low temperature. Due to the coexistence of different grain sizes in the sample, we confront the results with a description that involves two populations of B2-FeRh particles, and the existence of a discriminating size below which the magnetic order transition does not take place.

Introduction

Near the point of equiatomic composition, FeRh bulk alloys in the CsCl-type (B2) chemically ordered phase present a metamagnetic transition from the antiferromagnetic (AF) state at low temperature, with $\mu_{Fe} = 3.3\mu_B$ and no observable magnetic moment for Rh, to the ferromagnetic (F) state, with $\mu_{Fe} = 3.2\mu_B$ and $\mu_{Rh} = 0.9\mu_B$, above a critical temperature T_t of 370 K. This transition is accompanied by a 0.5% lattice parameter expansion.[1–4] The competition between both magnetic orders of FeRh occurs relatively close to room temperature (RT) and holds great potential for applications in magnetocaloric refrigeration due to its large negative magnetocaloric effect,[5–10] in ultrafast spintronics by heating FeRh with a laser to generate a spin current due to the uncompensated magnetic moment,[11–13] as well as in antiferromagnetic spintronics[14] and recording data.[15] Although the magnetic properties of FeRh nanostructures have been extensively studied for more than 25 years, the mechanism behind the AF to F transition is still widely debated and not well understood due to the strong correlation between structural, electronic and magnetic order in such nanoalloys.[16,17]

The presence of both magnetic orders has been experimentally observed in thin FeRh films, where the authors propose that the inner region becomes AF at low temperature while the surface remains F.[18] In nanostructures, defects and dislocations can also prevent the AF order in epitaxial FeRh films.[19,20] These works suggest that the AF order is very sensitive to the crystallinity and to the strain at surfaces and interfaces in thin films.

The AF/F phase coexistence in thick FeRh films epitaxially grown onto MgO(001) has also been experimentally observed and related to supercooled F grains as a result of the elastic lateral adaptation of the domains to the lattice mismatch with the substrate.[21] Even with the presence of the metamagnetic transition, a wide range of thermal hysteresis loop shapes has been reported.[16] A sharp transition has been observed in a 50 nm thick FeRh (001) film grown over MgO (001), closing the loop in ~40 K with similar shapes of the two branches,[18] while Loving *et al.* have reported a loop over ~300 K with a cooling-down branch significantly wider than the heating-up branch.[22] Nevertheless, a linear correlation between the transition temperature and the applied external field[13,23] is consistently observed, indicating that despite differences between the material microstructure and system dimensions, the intrinsic

[a]*Institut Lumière Matière, UMR 5306, Université Lyon 1-CNRS, Université de Lyon, F-69622 Villeurbanne Cedex, France. E-mail: guillermo.herrera.huerta@gmail.com, veronique.dupuis@univ-lyon1.fr*
[b]*Institut des Nanotechnologies de Lyon, CNRS UMR 5270 ECL INSA UCBL CPE, F-69621 Villeurbanne Cedex, France*
[c]*Synchrotron SOLEIL, L'Orme de Merisiers, 91190 Saint-Aubin, France*
[d]*European Synchrotron Radiation Facility, CS 40220, F-38043 Grenoble, France*
[e]*CNRS, INSA Lyon, Université Claude Bernard Lyon 1, MATEIS, UMR5510, F-69621 Villeurbanne, France*

† Electronic supplementary information (ESI) available. See DOI: https://doi.org/10.1039/d4nr00873a

properties of FeRh B2 alloys dominate this first order metamagnetic transition. Despite a lot of studies on thin films with low defect density,[19,20,24,25] the study of single B2 FeRh nanomagnets is rather rare. Some publications emphasized the strong interplay between crystal faceting, surface configuration, morphology and magnetic state in FeRh nanoparticles from DFT calculations and experimental studies.[26–28] By preparing FeRh nanocrystallites using low energy cluster beam deposition (LECBD) diluted in an amorphous carbon matrix, we demonstrated the persistence of the F order down to 3 K for size-selected clusters in B2 phase less than 10 nm in diameter.[29–31] We proposed that significant surface relaxation affecting the unit-cell parameter is responsible for the suppression of AF order even at very low temperature. This effect is associated with a significant surface-to-volume ratio, reaching up to approximately 70% in clusters of smallest nanosizes,[32] as already observed in other chemically ordered nanoalloys.[33] In this work, in order to enable a better understanding of the FeRh magnetic properties at the nanoscale, we have prepared a 150 nm thick FeRh film made of assembled nanoclusters preformed in gas phase. The film has been post-annealed to achieve chemical order in larger grains as possible by coalescence, resulting in a porous equiatomic B2 FeRh film with strongly correlated magnetic nanoalloyed grains. Our in-depth investigations of the metamagnetic phase transition reveals the correlation of magnetic properties with the nanometre size of FeRh grains.

Methods

Synthesis

The LECBD technique has been used to prepare a thick nanogranular FeRh sample. Briefly, a pulsed laser (Nd:YAG with wavelength λ = 532 nm, frequency of 20 Hz and 8 ns of duration) vaporizes the surface of an equiatomic FeRh target rod.[30,34] The plasma created at the rod's surface is then cooled down with an He gas stream at 30 mbar of partial pressure. This process initiates the nucleation and growth of nanoparticles in-flight, culminating in their deposition onto a substrate positioned within a connected UHV chamber. We report that nanoclusters directly deposited on a transmission electron microscopy grid present a size histogram with a log–normal distribution between 2 nm and 10 nm in diameter.[35] A thick FeRh sample has been UHV deposited on a Si wafer with a 150 nm nominal equivalent thickness. Then to limit subsequent oxidation, the sample was rapidly capped by ~15 nm amorphous carbon layer in UHV using a home-made evaporator (Patent Number WO/2014/191688). Previous works on as-prepared nanocluster films made in the same conditions have given ~60% of the bulk density,[36] close to a hard sphere model.[37]

After transfer in air, the sample was post-annealed in a UHV furnace at 500 °C for 2 h and then annealed again at 700 °C for 3 h to achieve the CsCl-like B2 phase. Due to coalescence occurring during thermal treatments, the size distribution of incident clusters is no longer anticipated to be present in the annealed self-assembled nanoalloyed sample.

Characterization

Atomic force microscopy (AFM). A topographic image has been performed in tapping mode at 70 kHz.

Transmission electron microscopy (TEM). A cross-section lamella of the FeRh film was made by focused ion beam (FIB) using the lift-out technique. The lamella was imaged using the high angle annular dark field (HAADF) contrast in scanning transmission electron microscopy (STEM) mode, in a FEI Titan ETEM G2, operated at 300 kV. Energy-dispersive X-ray (EDX) spectroscopy was performed in a Jeol JEM2100, equipped with an Oxford EDX spectrometer and operated at 200 kV.

Rutherford backscattering spectrometery (RBS). RBS was performed with $^4He^+$ ions of 2 MeV and a detector at 165° and 21 keV of resolution.

X-ray diffraction (XRD). Conventional specular XRD was performed in $\theta/2\theta$ geometry with Cu-Kα radiation.

Superconducting quantum interference device (SQUID) magnetometry. Magnetization measurements were performed using a commercial SQUID magnetometer (Quantum Design MPMS 5XL) in the range of temperature (2–400 K) and for magnetic field direction parallel to the sample surface up to 5 T.

X-ray absorption spectroscopy (XAS) and X-ray magnetic circular dichroism (XMCD). XAS and XMCD experiments were performed at the Rh $M_{2,3}$-edge and Fe $L_{2,3}$-edges on the soft X-ray DEIMOS beamline at SOLEIL synchrotron (Saint-Aubin, France), and at the Fe K and at the Rh $L_{2,3}$-edges on the hard X-ray ID12 beamline at ESRF synchrotron (Grenoble, France). More details for each beamline are available elsewhere.[38,39] The specimens were transported in a sealed desiccator under primary vacuum, from the PLYRA synthesis facility (UHV) to the synchrotron beamlines where they were fixed on sample plates (atmospheric pressure) prior to insertion in the beamline chambers (UHV). At DEIMOS, the total electron yield (TEY) signal was collected and used to estimate the Fe magnetic moment, under a 6 T magnetic field parallel to the X-ray beam along the normal to the sample surface plane. The total fluorescence yield (TFY) probes a much deeper portion of the sample (~100 nm from the surface) and was also collected at the same time. At ID 12, the sample was placed under a 7 T magnetic field parallel to the X-ray beam, which was aligned with a 15° angle with respect to the sample surface. In the case of hard X-rays, the TFY signal was collected and used to interpret X-ray absorption near edge structures (XANES) and to estimate the Rh induced magnetic moment at the $L_{2,3}$ edge. As the accessible temperature range is 4–320 K on both beam lines, XMCD experiments were conducted under an applied magnetic field as high as possible to increase the probability to induce the metamagnetic transition.

Results and discussion

Morphology and microstructure

The microstructure of the FeRh film was investigated at the nanoscale, with a topographic view of the sample surface using AFM (Fig. 1a), and with a lateral view of a cross-section

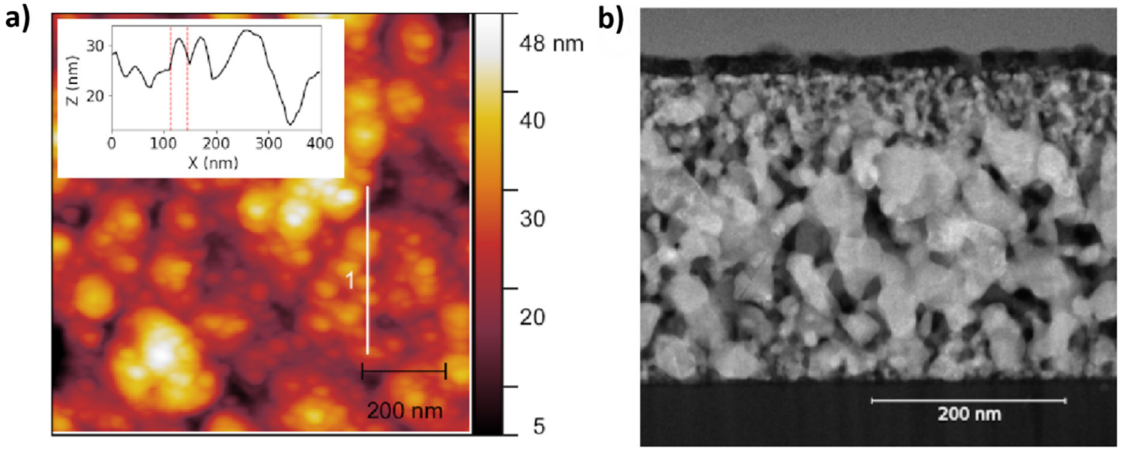

Fig. 1 AFM top view of the FeRh nanocluster assembled film with 150 nm nominal thickness measured in tapping mode (a), and topography profile along line 1 (white) with a 30 nm length dome delimited with the red vertical dotted lines (inset). STEM-HAADF lateral view on a cross-section lamella of the FeRh nanocluster assembled film (b).

lamella of the sample using STEM-HAADF (Fig. 1b). Both AFM and STEM-HAADF images reveal clearly that the film conserves a granular structure after the thermal treatment. The STEM-HAADF image shows that the sample is apparently ~310 nm thick due to high film porosity compared to the 150 nm nominal thickness determined from Quartz Crystal Microbalance that monitors total mass deposition assuming full film density. In addition, it is significant that the annealing led to a large nanoparticle size dispersion: the nanoparticles are ~10 nm in diameter in the upper ~60 nm part of the film and close to the interface with the substrate, while nanoparticles are ~100 nm or greater in diameter in the center of the film. Given the large porosity of the film, the STEM-HAADF image does not allow to obtain a precise size dispersion of the nanoparticles, but instead highlights the heterogeneous spatial distribution between the surface and middle of the film as well as at the interface with the substrate, as shown in Fig. 1b. The AFM image also reveals height fluctuations and lateral coalescence of nanoparticles upon annealing (Fig. 1a). These observations suggest the coalescence of FeRh nanoparticles, which occurs preferentially in the middle of the film. Such complex 3D microstructure with a large porosity leads to a higher apparent thickness for the annealed sample compared to the nominal value estimated from quartz balance during cluster deposition.

Chemical composition and crystallography

The alloyed Fe1 : Rh1 composition of larger grains is clearly observable in ESI (Fig. S1†) from an EDX map performed on the same cross section lamella as the STEM-HAADF. RBS also reveals an Fe/Rh relative concentration of 50%/50% ± 4% (see ESI Fig. S2†), which overlaps, within the error, the range of equiatomic concentration needed for the occurrence of the metamagnetic B2 FeRh phase transition.[40]

XRD on the annealed sample (3 h at 700 °C) showed that the FeRh CsCl-like B2 phase with a = 2.98 Å (bulk value)[2] is dominant in the sample as shown in Fig. 2a. However, the film still contains a minor quantity of chemically disordered A1 FeRh phase with a = 3.77 Å, which is ~2% larger than the lattice parameter reported for the bulk.[41] By using the Scherrer formula for the XRD peaks of FeRh A1 (111) and FeRh B2 (011) with the shape factor 0.9 of the sphere,[42] a ~14 nm size was estimated for the crystallites in A1 phase and a ~27 nm size for the crystallites in B2 phase (Fig. 2b) from the full width at half maximum (FWHM) of the respective diffraction peaks. The main peak of Fe_3O_4 (311),[43] which has a low intensity here, suggests the oxidation of iron in a minor proportion. In the following, we will see that the weak magnetic contribution of the FeRh A1 phase can be neglected compared to the high magnetic moment expected for the FeRh B2 majority nanoparticles.[31]

Global magnetic measurements

SQUID magnetization measurements were performed on the as-prepared sample and after several UHV annealing cycle durations at two temperatures namely 500 °C and 700 °C. For the as-prepared sample initially in the A1 phase, we obtained a very weak magnetic signal (as seen from $m(T)$ under 2.5 T in Fig. 3). This is consistent with the paramagnetic nature of bulk FeRh A1, and similar observations have been reported for as prepared continuous films.[44] While a 2 h annealing at 500 °C slightly increases the magnetic signal, it is only after a 3 h annealing at 700 °C that a strong magnetic signal is obtained. Moreover, we detect a metamagnetic phase transition that does not evolve after a further 7 h annealing at 700 °C. More precisely, the dependence of the magnetic moment with temperature, $m(T)$, has been considered when cooling (heating) the 700 °C annealed sample from 400 K. Fig. 3 displays the $m(T)$ curves measured under magnetic fields ranging from 0.1 T to 5 T, all presenting a partial metamagnetic phase transition around room temperature. Regardless of the applied magnetic field, $m(T)$ curves are characterized by (i) a large thermal hys-

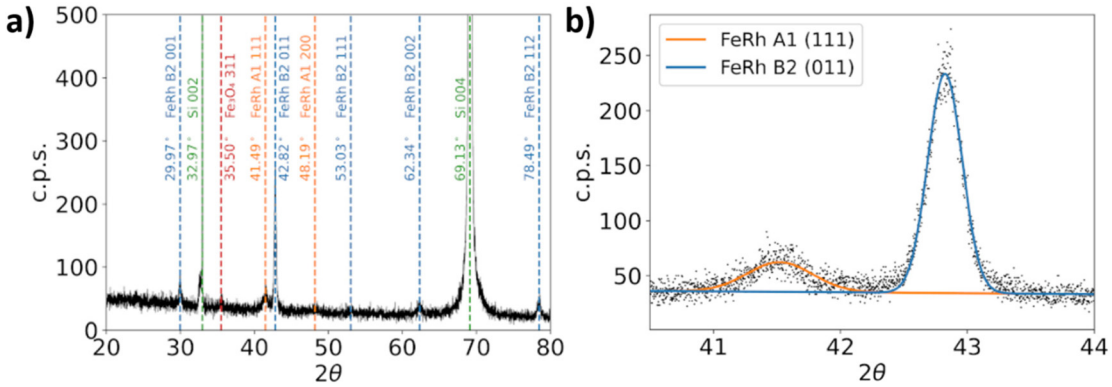

Fig. 2 Specular XRD pattern of the FeRh nanocluster assembled film with labelled peak positions of FeRh A1 phase (orange), FeRh B2 phase (blue), Si (green) and Fe_3O_4 (red) (a). Magnification of the XRD pattern in the region of FeRh A1 (111) and FeRh B2 (011) peaks with Gaussian fits using the Scherrer formula with shape factor 0.9 (b).

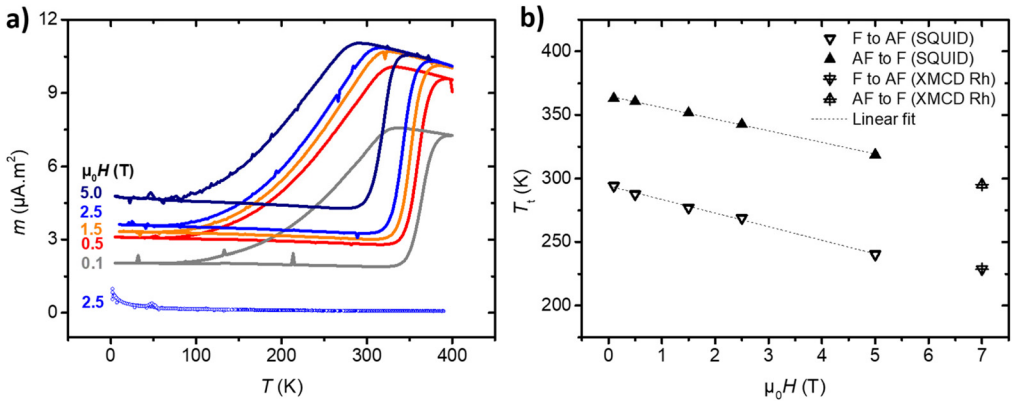

Fig. 3 (a) SQUID magnetometry between 4 K and 400 K for external magnetic field of 0.1 T (grey), 0.5 T (red), 1.5 T (orange), 2.5 T (blue) and 5.0 T (dark blue). The $m(T)$ curves measured after annealing are represented with full symbols, and compared to the $m(T)$ curve measured at 2.5 T in the as prepared state (open symbols). (b) The transition temperature determined from SQUID $m(T)$ curves, in the cooling-down branch (upside-down open triangles) and the heating-up branch (filled triangles) calculated as the maximum of the first derivative. The dashed lines are best linear fits. The points at 7 T are obtained from the XMCD signal on Rh edge.

teresis extended over more than 200 K, (ii) similar asymmetry with a smooth transition from F to AF states upon cooling, and a sharper transition from AF to F states upon heating, and (iii) a temperature range from 2 K to 50 K where the $m(T)$ curves are reversible. At such low temperature, the system displays a small coercivity, reflecting the persistence of a residual ferromagnetic contribution. In other words, only a fraction of the film transits into the AF state upon cooling. Besides, while the high temperature F signal saturates at around 1.5 T, we observe that the low temperature residual signal is still increasing with the applied magnetic field. This non saturating contribution has been attributed to spin canting effects in the AF Fe sublattice.[45] In order to estimate the amount of the residual ferromagnetic phase, we compare the low temperature magnetic moment at 1.5 T with the maximum high temperature moment. This procedure assumes that: (i) the AF signal (spin canting) at such a field is negligible with respect to the F phase, and (ii) the F signal is saturated and does not vary with temperature in the 0–300 K range, and (iii) the magnetic contribution of minor A1 phase is fully negligible. We find that ~27% of the ferromagnetic signal does not vanish: in other words, ~27% of the B2 FeRh remains in the F phase at low temperature.

A substantial distribution in nanograin size, porosity, and potential dispersion around the equiatomic composition could contribute to the observed broad thermal hysteresis. Interestingly, despite the nanogranular microstructure of the presently characterised thick film, the magnetic field dependence of the transition temperature closely resembles that observed in continuous FeRh films[23] and wires,[13] *i.e.* nearly linear with a slope of −9.1 K/T as seen in Fig. 3b. Let us emphasize that the transition temperature, defined as the maximum of the first derivative, is different for the heating and cooling branches.

According to Biswas *et al.*,[46] the broad metamagnetic transition could be attributed to surface defects present in a nanogranular system that slow down the kinetics of growth of the new phase. Motyčková *et al.*[28] report similar thermal

magnetization curves on self-assembled of sub-micron FeRh nanoislands capable of sustaining a supercooled state at about 150–200 K below their transition temperature to FM states. They suggest that as the size of FeRh nanostructures decreases, the lack of availability of nucleation sites for the AF phase to be nucleated during cooling causes supercooling, stabilizing the F phase below its phase transition temperature. The asymmetrical transition (sharp transition from AF to F and smooth transition from F to AF) can be explained by the fact that an individual grain is submitted to the net stray field created by all neighbouring F grains, which favors this grain to remain in the F state.

In our case, the local field hypothesis cannot explain the transition temperature range in the cooling. Indeed several tens of teslas would be required to shift the transition temperature by more than 100 K. Note that the asymmetry and width of phase transition differ from the ones observed for a 150 nm-thick continuous B2 FeRh film[44] but also for a 50 nm-thick film with controlled disorder[19] (in this case the heating branch is also broadened and shifted). However, the shape of the transition is comparable to the thinnest film of Han *et al.*[47] (3 nm equivalent thickness) corresponding to 35 nm diameter grains.

From Fig. 3, the field dependence of the transition suggests that at a given temperature in the transition range, one can trigger the F to AF transition of some FeRh grains by reducing the external field or conversely, trigger the transition from AF to F states by increasing the external field. To confirm this feature, we varied the applied magnetic field at discrete temperatures. Thus $m(T)$ was measured at 1.5 T, with interruptions to perform $m(H)$ loops at 250 K in the cooling-down branch, then at 250 K and at 325 K in the heating-up branch (See Fig. 4). Each $m(H)$ loop starts with increasing the magnetic field H from 1.5 T to 5 T, then sweeping H back and forth between 5 T and −5 T, and finally returning from 5 T to 1.5 T.

These experiments show that at 250 K in the cooling branch, the field switch off triggers the F/AF transition of a limited fraction of nanograins, while no AF/F transition occurs in the heating branch by changing H. In contrast, at the beginning of the heating branch transition, the increase of H induces the AF/F transition of a larger fraction of nanograins (Δm is seven times larger than previously). Note that we retrieve the $m(T)$ value of the heating branch for 5 T. We observe that after each interruption, $m(T)$ is constant over a temperature range ΔT in agreement with the T_t field dependence (Fig. 3b).

To explore further the coexistence of both magnetic order contributions, we conducted element-specific magneto-optical spectroscopy at the L-edges of both Rh and Fe elements by using two synchrotron facilities, ESRF for hard X-ray and SOLEIL for soft X-ray energy, respectively.

Element-specific magnetic measurements

Hard X-ray absorption spectroscopy. XAS and XMCD measurements were performed at the Fe K-edge (~7113 eV) and Rh $L_{2,3}$-edges (~3146 eV and 3004 eV) in TFY mode. Using hard X-rays provides a more volume sensitive approach compared to soft X-rays. A clear XANES signature evolution at both edges has been observed from the as-prepared sample in chemically disordered FCC A1 phase to the 700 °C annealed sample, mostly in B2 phase (see ESI Fig. S3a and S3b†).[48–51] Moreover, the XMCD signal recorded at the Rh L_2-edge at 320 K under 7 T on the as-prepared sample has been found negligible compared to the clear dichroic signal obtained on the 700 °C-annealed FeRh sample (see ESI Fig. S3c†). For the annealed sample, by neglecting the magnetic dipole term T_z, we respectively extracted an induced Rh magnetic moment of $0.16\mu_B$ at 4 K and of $0.65\mu_B$ at 320 K within 10% of error from the XMCD signal measured at the Rh L_2-edge under 7 T (Fig. 5a). The absolute value of the orbital to spin ratio, which is independent of the number of 4d holes,[52,53] has been found equal to 8% and does not vary with the temperature. The magnetic moment curves obtained on the annealed sample as a function of applied magnetic field and as a function of temp-

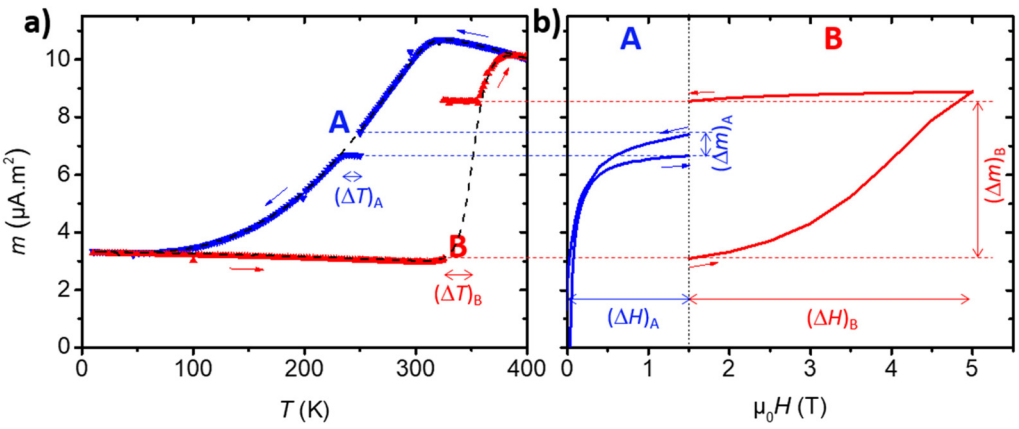

Fig. 4 (a) $m(T)$ curves measured at a magnetic field of 1.5 T. The dashed $m(T)$ curve is measured under continuous temperature sweeping. The blue $m(T)$ curve is measured upon cooling, and interrupted with a $m(H)$ loop at 250 K (step A). The red $m(T)$ curve is measured upon heating, and interrupted with a $m(H)$ loop at 325 K (step B). (b) Irreversible m variation, when decreasing the field H over $(\Delta H)_A$ (step A), and when increasing the field Hover $(\Delta H)_B$ (step B).

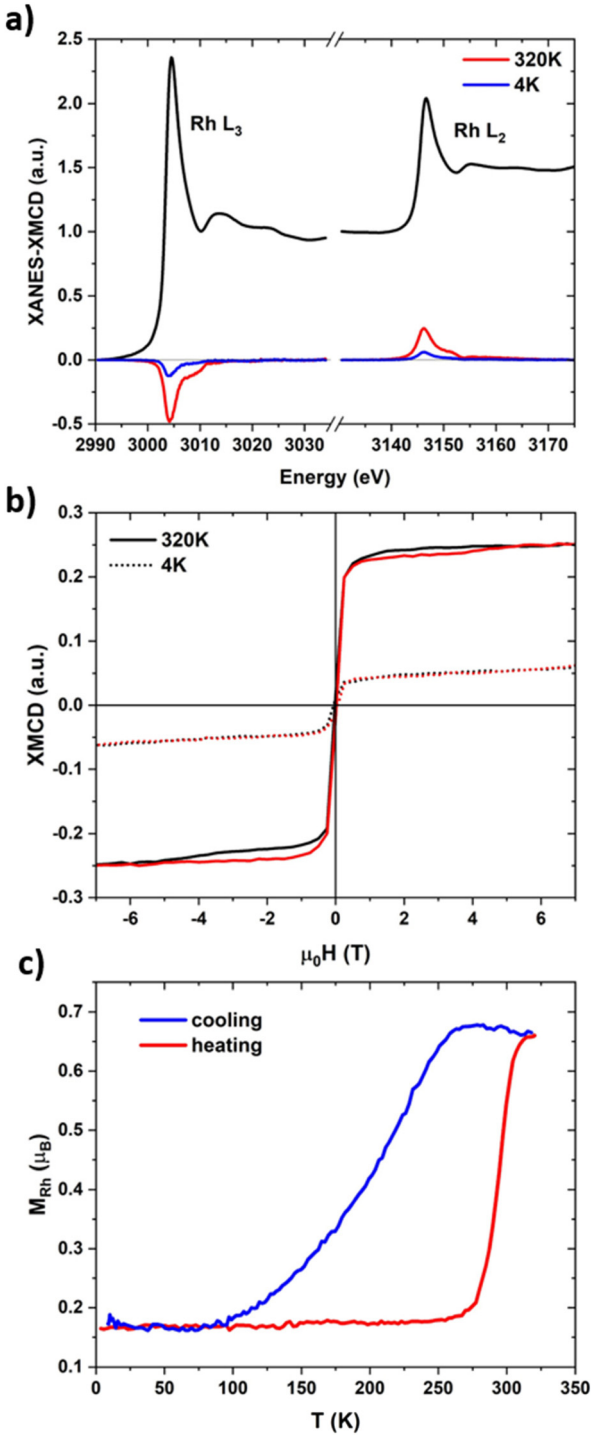

Fig. 5 XAS and XMCD in the hard X-ray regime measured on the annealed FeRh nanocluster assembled film in TFY mode at the Rh L-edge under 7 T and 15° grazing incidence leading to a total magnetic moment of 0.16μ_B at 4 K and 0.65μ_B at 320 K (a). XMCD signal taken as the maximum XAS value at the L_2-edge *versus* the applied magnetic field (b). Temperature dependence of the Rh total magnetic moment measured from thermal XMCD evolution under 7 T (c).

erature (Fig. 5b and c, respectively) have been recorded from the XMCD maximum value taken at the Rh L_2-edge. On the one hand, the comparison between field-dependent XMCD curves in Fig. 5b shows a small saturated value consistent with the fraction of B2 FeRh that remains in the F phase at 4 K, while an obvious irreversibility in the saturation regime of the $m(H)$ curves at 320 K could be explained by the combination of the weak anisotropy of the AF phase and the soft F phase.[44] On the other hand, it is worth highlighting that the thermal evolution of the induced Rh magnetic moment (Fig. 5c) closely follows the magnetization curve obtained from SQUID magnetometry across the entire sample (Fig. 3). In particular, both transition temperatures found equal to ~270 K in the heating-up branch and ~250 K in the cooling-down branch from XMCD are in very good agreement with the values 274 K and 256 K expected at 7 T from the SQUID linear extrapolation (see Fig. 3b).

Bear in mind that Rh atoms are expected to have a null magnetic moment in A1 and B2 FeRh AF phases and a 0.9μ_B moment value in the F bulk phase. For our annealed sample, the mean Rh magnetic moment estimated at high temperature, where only the B2 F phase should give a signal, is equal to ~72% of the bulk value. This can be attributed to local variations of composition and/or to the presence of minor A1 phase, in agreement with RBS and XRD measurements and considering that the remainder ~28% of Rh atoms have a negligible magnetic signal. In this case, the small Rh residual magnetic moment measured at low temperature suggests that ~25% of the B2 FeRh component is not switching to the AF phase even at very low temperature. Remarkably, this percentage is in full agreement with the one estimated from SQUID measurements. Note that, in the AF B2 phase, contrary to the Fe contribution, there is no spin canting expected for Rh since it has no magnetic moment. Therefore, as pure Rh is not magnetic, these results indicate that the Rh magnetic moment of the F phase is induced by strong hybridization with Fe.

Soft X-ray absorption spectroscopy. XAS and XMCD measurements were performed at the Fe $L_{2,3}$-edges (~722 and 709 eV) on the sample annealed at 700 °C. The XMCD signal at the Rh $M_{2,3}$-edges with no multiplet structures (see ESI Fig. S4a†) is characteristic of a fully metallic Rh, while the Fe $L_{2,3}$ XANES and XMCD signals show a double peak (see ESI Fig. S4b†), which is characteristic of Fe_3O_4 and in agreement with the small peak at 35° visible in the XRD pattern (Fig. 2a).[54] This reveals some iron oxidation despite the carbon capping. Nevertheless, this iron oxide is probably in the form of a thin amorphous or weakly crystalline magnetite Fe_3O_4 shell at the surface of nanoparticles, which passivates the bimetallic core as already observed for Fe-based clusters.[55,56]

To address the issue of iron oxide contribution observed at the Fe $L_{2,3}$-edges, the sample was *in situ* annealed at 600 °C for 5 h in UHV conditions, prior to new XAS/XMCD measurements as reported in Fig. 6a at 4 K and 320 K under 6 T. The XAS and XMCD signals show less oxide contributions. By using sum rules, we obtain a Fe magnetic moment of 1.2μ_B at 4 K and 1.6μ_B at 320 K. This small difference in magnetic moment is visible in the XMCD plot as a function of the applied magnetic field in Fig. 6b. At high temperature, where a full F phase is expected, the value of 1.6μ_B only corresponds to half of the

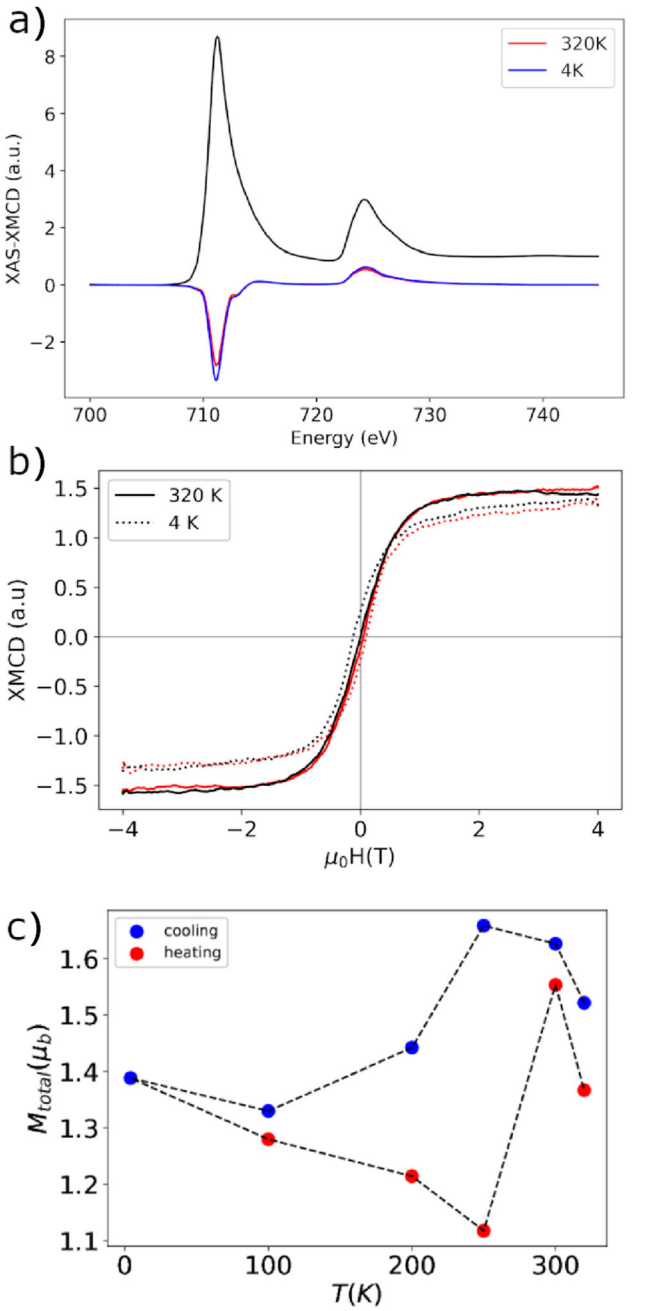

Fig. 6 XAS and XMCD in the soft X-ray regime measured on the annealed FeRh nanocluster assembled film at the Fe L-edge in TEY mode under 6 T and perpendicular incidence leading to a total magnetic moment of 1.4μ_B at 4 K and 1.5μ_B at 320 K (a). XMCD signal taken as the max XAS value at the Fe L_3 edge *versus* the applied magnetic field (b). Temperature dependence of the Fe total magnetic moment measured from the thermal XMCD evolution under 6 T (c).

expected Fe magnetic moment in the bulk B2 F phase, suggesting that the *in situ* reduction only led to a partially metallic phase. Nevertheless, a partial metamagnetic transition has been obtained up to 85% (resp. 75%) in TEY (resp. TFY) mode, as shown in Fig. 6c (resp. ESI Fig. S5†). Despite a larger non-switchable component, the curve shape and transition temperature range roughly look like the global $m(T)$ curve obtained from SQUID measurement. Since the TEY signal is highly surface sensitive, with a sampling depth of ~5–10 nm in the soft X-ray regime, whereas the TFY signal is limited to the first ~100 nm in depth, this result suggests that a non-switchable component is associated to small size nanoparticles located at the film's surface/interface where oxidation limits edge grain growth and nanoparticle coalescence upon annealing, in agreement with the STEM-HAADF image and EDX maps shown in Fig. 1 and Fig. S1.† Notice that such different grain size distribution mentioned as gradient-structured metals and alloys has been observed in a large variety of nanocrystalline materials structures due to distinct strain zones and specific thermodynamics during coarsening.[57]

Conclusion

In summary, using soft and hard X-ray absorption measurements combined with microstructural characterization, we provide a complete description of the local magnetic behaviour of a thick B2 FeRh film made of a nanocluster assembly. From XMCD at the Fe $L_{2,3}$ and Rh $L_{2,3}$-edges, we show that the XAS/XMCD evolution with temperature at both edges corresponds to the global metamagnetic transition obtained from SQUID magnetometry. This combination of experimental techniques provides convincing evidence that the residual ferromagnetic component observed at low temperatures does not stem from elemental segregation or sample contamination; but rather corresponds to a remaining F FeRh B2 phase contribution that we attribute to finite size effects in nanogranular films. We thus demonstrate that the metamagnetic transition in a nanogranular FeRh film can be separated into two components: a non-switchable contribution (*i.e.*, remaining ferromagnetic at low temperature), which is associated to alloyed nanomagnets typically smaller than 20 nm in size, and a switchable component associated to larger nanoparticles, which present the AF/F transition near room temperature. This comprehensive model is validated by the present experimental evidences of small B2 FeRh nanoparticles located at the surface of the film while larger nanoparticles are found in the centre of the film. Moreover as the metamagnetic FeRh phase transition could induce interesting change in thermal conductivity, thermoelectric (TE) materials including FeRh nanomagnet could be studied to improve the TE figure of merit in the context of waste energy conversion to electricity.[58]

Author contributions

This work is part of the G. H. PhD thesis (Lyon 2023) under V.D. and I.C-I. co-supervision and financial support of the VOLCONANO ANR-19-CE09–0023 coordinated by V.D. with I.C-I., P.O. and M.B. as partners. G.H. performed all material characterizations and analysis presented in this manuscript while A.R. synthesized the first FeRh sample of interest at the

end of his PhD thesis (Lyon 2017) under the co-supervision of V.D. and A.T. L.B., O.B. and C.A. assisted experimental developments for LECBD synthesis and *in situ* surface analysis at PLYRA. B.C. executed RBS measurements and simulations, while M.B. and N.B. respectively, performed STEM/HAADF and TEM/EDX maps and analysis with G.H. SQUID measurements have been performed by G.H. and discussed with D.L R., A.T., F.T. and V.D. XAS/XMCD studies on synchrotrons and analysis where carried out by E.O., P.O., F.W. and A.R. as beam line scientists and local contacts, of P.S. and of S.G. as Post Doc supported by VOLCONANO and of the participation of G. H., D.L R., F.T., M.B., P.R.R. and V.D. during experiments. G. H., M.B., D.L R. and V.D. specifically wrote the initial draft, further improved with F.T. and A.T., while all authors contributed to the final review of the submitted manuscript.

Conflicts of interest

The authors declare no competing financial interest.

Acknowledgements

The authors are very grateful to the ILMTECH platform for cluster synthesis at PLYRA and SQUID measurements at CML, to A. Piednoir from iLM for AFM measurements, to J. Penuelas from Lyon Nanotechnology Institute for XRD measurements on the FeRh thick samples, and for their technical support and fruitful discussions. The STEM work was performed at the Consortium Lyon-St-Etienne de microscopie. XAS and XMCD experiments were performed at SOLEIL (proposal number 20220197) and ESRF (proposal number HC-4794) synchrotrons. We are grateful to SOLEIL and ESRF staff for their assistance during the experiments and smoothly running the facility. Financial support is acknowledged from the International Research Network (IRN)/Groupement de Recherches International (GDRI) on Nanoalloys and from ANR to the ANR-19-CE09-0023 VOLCONANO project. For the purpose of open access, the authors have applied a CC-BY public copyright licence to any Author Accepted Manuscript version arising from this submission.

References

1 M. Fallot, *Ann. Phys.*, 1938, **11**, 291–332.
2 G. Shirane, R. Nathans and C. W. Chen, *Phys. Rev.*, 1964, **134**, A1547–A1553.
3 V. L. Moruzzi and P. M. Marcus, *Phys. Rev. B: Condens. Matter Mater. Phys.*, 1992, **46**, 2864–2873.
4 M. R. Ibarra and P. A. Algarabel, *Phys. Rev. B: Condens. Matter Mater. Phys.*, 1994, **50**, 4196–4199.
5 D. W. Cooke, F. Hellman, C. Baldasseroni, C. Bordel, S. Moyerman and E. E. Fullerton, *Phys. Rev. Lett.*, 2012, **109**, 255901.
6 S. Nikitin, G. Myalikgulyev, A. Tishin, M. Annaorazov, K. Asatryan and A. Tyurin, *Phys. Lett. A*, 1990, **148**, 363–366.
7 Y. Liu, L. Phillips, R. Mattana, M. Bibes, A. Barthélémy and B. Dkhil, *Nat. Commun.*, 2016, **7**, 11614.
8 Y. Spichkin and A. Tishin, *J. Alloys Compd.*, 2005, **403**, 38–44.
9 M. Manekar and S. B. Roy, *J. Phys. D: Appl. Phys.*, 2008, **41**, 192004.
10 E. Stern-Taulats, A. Planes, P. Lloveras, M. Barrio, J.-L. Tamarit, S. Pramanick, S. Majumdar, C. Frontera and L. Mañosa, *Phys. Rev. B: Condens. Matter Mater. Phys.*, 2014, **89**, 214105.
11 J.-U. Thiele, M. Buess and C. H. Back, *Appl. Phys. Lett.*, 2004, **85**, 2857–2859.
12 G. Ju, J. Hohlfeld, B. Bergman, R. J. M. van de Veerdonk, O. N. Mryasov, J.-Y. Kim, X. Wu, D. Weller and B. Koopmans, *Phys. Rev. Lett.*, 2004, **93**, 197403.
13 M. Grimes, V. Sazgari, S. Parchenko, J. Zhou, Y. Soh, L. J. Heyderman, T. Thomson and V. Scagnoli, *J. Phys. D: Appl. Phys.*, 2023, **56**, 485002.
14 Y. Wang, M. M. Decker, T. N. G. Meiner, X. Chen, C. Song, T. Grunbaum, W. Zhao, J. Zhang, L. Chen and C. H. Back, *Nat. Commun.*, 2020, **11**, 275.
15 J.-U. Thiele, S. Maat and E. E. Fullerton, *Appl. Phys. Lett.*, 2003, **82**, 2859–2861.
16 L. H. Lewis, C. H. Marrows and S. Langridge, *J. Phys. D: Appl. Phys.*, 2016, **49**, 323002.
17 C. Gatel, B. Warot-Fonrose, N. Biziere, L. Rodŕguez, D. Reyes, R. Cours, M. Castiella and M. Casanove, *Nat. Commun.*, 2017, **8**, 15703.
18 F. Pressacco, V. Uhlíř, M. Gatti, A. Bendounan, E. E. Fullerton and F. Sirotti, *Sci. Rep.*, 2016, **6**, 22383.
19 B. Eggert, A. Schmeink, J. Lill, M. O. Liedke, U. Kentsch, M. Butterling, A. Wagner, S. Pascarelli, K. Potzger, J. Lindner, T. Thomson, J. Fassbender, K. Ollefs, W. Keune, R. Bali and H. Wende, *RSC Adv.*, 2020, **10**, 14386–14395.
20 D. G. Merkel, A. Lengyel, D. L. Nagy, A. Németh, Z. E. Horáth, C. Bogdán, M. A. Gracheva, G. Hegedűs, S. Sajti, G. Z. Radnócz and E. Szilágyi, *Sci. Rep.*, 2020, **10**, 13923.
21 J. A. Arregi, F. Ringe, J. Hajduček, O. Gomonay, T. Molnár, J. Jaskowiec and V. Uhlíř, *J. Phys.: Mater.*, 2023, **6**, 034003.
22 M. Loving, F. Jimenez-Villacorta, B. Kaeswurm, D. A. Arena, C. H. Marrows and L. H. Lewis, *J. Phys. D: Appl. Phys.*, 2013, **46**, 162002.
23 S. Maat, J.-U. Thiele and E. E. Fullerton, *Phys. Rev. B: Condens. Matter Mater. Phys.*, 2005, **72**, 214432.
24 R. O. Cherifi, V. Ivanovskaya, L. C. Phillips, A. Zobelli, I. C. Infante, E. Jacquet, V. Garcia, S. Fusil, P. R. Briddon, N. Guiblin, A. Mougin, A. A. Ünal, F. Kronast, S. Valencia, B. Dkhil, A. Barthélémy and M. Bibes, *Nat. Mater.*, 2014, **13**, 345–351.
25 J. L. Warren, C. W. Barton, C. Bull and T. Thomson, *Sci. Rep.*, 2020, **10**, 4030.
26 M. Liu, P. Benzo, H. Tang, M. Castiella, B. Warot-Fonrose, N. Tarrat, C. Gatel, M. Respaud, J. Morillo and M. J. Casanove, *EPL*, 2016, **116**, 27006.

27 P. Benzo, S. Combettes, C. Garcia, T. Hungria, B. Pécassou and M.-J. Casanove, *Cryst. Growth Des.*, 2020, **20**, 4144–4149.
28 L. Motyčková, J. A. Arregi, M. Staňo, S. Průša, K. Částková and V. Uhlíř, *ACS Appl. Mater. Interfaces*, 2023, **15**, 8653–8665.
29 A. Hillion, A. Cavallin, S. Vlaic, A. Tamion, F. Tournus, G. Khadra, J. Dreiser, C. Piamonteze, F. Nolting, S. Rusponi, K. Sato, T. J. Konno, O. Proux, V. Dupuis and H. Brune, *Phys. Rev. Lett.*, 2013, **110**, 087207.
30 V. Dupuis, A. Robert, A. Hillion, G. Khadra, N. Blanc, D. Le Roy, F. Tournus, C. Albin, O. Boisron and A. Tamion, *Beilstein J. Nanotechnol.*, 2016, 1850–1860.
31 G. Herrera, A. Robert, V. Dupuis, N. Blanchard, O. Boisron, C. Albin, L. Bardotti, D. Le Roy, F. Tournus and A. Tamion, *Eur. Phys. J.: Appl. Phys.*, 2022, **97**, 32.
32 R. Van Hardeveld and F. Hartog, *Surf. Sci.*, 1969, **15**, 189–230.
33 V. Dupuis, N. Blanc, L. E. Díaz-Sánchez, A. Hillion, A. Tamion, F. Tournus and G. M. Pastor, *Eur. Phys. J.*, 2013, **86**, 1850–1860.
34 A. Perez, P. Melinon, V. Dupuis, P. Jensen, B. Prevel, J. Tuaillon, L. Bardotti, C. Martet, M. Treilleux, M. Broyer, M. Pellarin, J. L. Vaille, B. Palpant and J. Lerme, *J. Phys. D: Appl. Phys.*, 1997, **30**, 709–721.
35 V. Dupuis, A. Hillion, A. Robert, A. Robert, O. Loiselet, G. Khadra, P. Capiod, C. Albin, O. Boisron, D. Le Roy, L. Bardotti, F. Tournus and A. Tamion, *J. Nanopart. Res.*, 2018, **20**, 128.
36 J. Perez, V. Dupuis, J. Tuaillon, A. Perez, V. Paillard, P. Melinon, M. Treilleux, L. Thomas, B. Barbara and B. Bouchet-Fabre, *J. Magn. Magn. Mater.*, 1995, **145**, 74–80.
37 S. Torquato, T. M. Truskett and P. G. Debenedetti, *Phys. Rev. Lett.*, 2000, **84**, 2064–2067.
38 P. Ohresser, E. Otero, F. Choueikani, K. Chen, S. Stanescu, F. Deschamps, T. Moreno, F. Polack, B. Lagarde, J. P. Daguerre, F. Marteau, F. Scheurer, L. Joly, J. P. Kappler, B. Muller, O. Bunau and P. Sainctavit, *Rev. Sci. Instrum.*, 2014, **85**, 013106.
39 A. Rogalev, F. Wilhelm, K. Kummer and N. Brookes, *Synchrotron Radiat. News*, 2020, **33**, 30–34.
40 L. J. Swartzendruber, *Bull. Alloy Phase Diagrams*, 1984, **5**, 456–462.
41 J. M. Lommel and J. S. Kouvel, *J. Appl. Phys.*, 1967, **38**, 1263–1264.
42 A. L. Patterson, *Phys. Rev.*, 1939, **56**, 978–982.
43 D.-W. Lee, H. Fatima and K.-S. Kim, *J. Nanosci. Nanotechnol.*, 2018, **18**, 1414–1418.
44 J. Cao, N. T. Nam, S. Inoue, H. Y. Y. Ko, N. N. Phuoc and T. Suzuki, *J. Appl. Phys.*, 2008, **103**, 07F501.
45 B. R. McGrath, R. E. Camley and K. L. Livesey, *Phys. Rev. B*, 2020, **101**, 014444.
46 A. Biswas, S. Gupta, D. Clifford, Y. Mudryk, R. Hadimani, R. Barua and V. K. Pecharsky, *J. Alloys Compd.*, 2022, **921**, 165993.
47 G. C. Han, J. J. Qiu, Q. J. Yap, P. Luo, D. E. Laughlin, J. G. Zhu, T. Kanbe and T. Shige, *J. Appl. Phys.*, 2013, **113**, 17C107.
48 N. Blanc, L. E. Díaz-Sánchez, A. Y. Ramos, F. Tournus, H. C. N. Tolentino, M. De Santis, O. Proux, A. Tamion, J. Tuaillon-Combes, L. Bardotti, O. Boisron, G. M. Pastor and V. Dupuis, *Phys. Rev. B: Condens. Matter Mater. Phys.*, 2013, **87**, 155412.
49 F. Baudelet, A. Fontaine, G. Tourillon, D. Guay, M. Maurer, M. Piecuch, M. F. Ravet and V. Dupuis, *Phys. Rev. B: Condens. Matter Mater. Phys.*, 1993, **47**, 2344–2352.
50 A. Smekhova, D. Ciuculescu, P. Lecante, F. Wilhelm, C. Amiens, A. Rogalev and B. Chaudret, *IEEE Trans. Magn.*, 2008, **44**, 2776–2779.
51 A. Aubert, K. Skokov, G. Gomez, A. Chirkova, I. Radulov, F. Wilhelm, A. Rogalev, H. Wende, O. Gutfleisch and K. Ollefs, *IEEE Trans. Instrum. Meas.*, 2022, **71**, 1–9.
52 B. Thole, P. Carra, F. Sette and G. van der Laan, *Phys. Rev. Lett.*, 1992, **68**, 1943.
53 P. Carra, B. Thole, M. Altarelli and X. Wang, *Phys. Rev. Lett.*, 1993, **70**, 694.
54 A. Papaefthimiou, F. Tournus, A. Hillion, G. Khadra, D. Teschner, A. Knop-Gericke, V. Dupuis and S. Zafeiratos, *Chem. Mater.*, 2014, **26**, 1553–1560.
55 M. Sassi, C. I. Pearce, P. S. Bagus, E. Arenholz and K. M. Rosso, *J. Phys. Chem. A*, 2017, **121**, 7613–7618.
56 W. Karim, A. Kleibert, U. Hartfelder, A. Balan, J. Gobrecht, J. A. van Bokhoven and Y. Ekinci, *Sci. Rep.*, 2016, **6**, 18818.
57 W. Ji, R. Zhou, P. Viveganantha, M. See Wu, H. Gao and K. Zhou, *Prog. Mater. Sci.*, 2023, **140**, 101194.
58 C. Liu, C. Wu, Y. Zhao, Z. Chen, T.-L. Ren, Y. Chen and G. Zhang, *Phys. Rep.*, 2024, **1058**, 1–32.